Food Chemistry 424 (2023) 136323

Contents lists available at ScienceDirect

Food Chemistry

journal homepage: www.elsevier.com/locate/foodchem

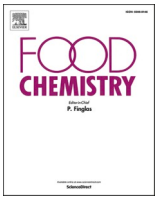

Highly sensitive and selective Sb_2WO_6 microspheres in detecting VOC biomarkers in cooked rice: Experimental and density functional theory study

Chao Zhang [a,*], Zichen Zheng [a], Kewei Liu [a], Marc Debliquy [b], Qiaoquan Liu [c]

[a] College of Mechanical Engineering, Yangzhou University, Yangzhou 225127, PR China
[b] Service de Science des Matériaux, Faculté Polytechnique, Université de Mons, Mons 7000, Belgium
[c] Key Laboratory of Crop Genetics and Physiology of Jiangsu Province, Co-Innovation Center for Modern Production Technology of Grain Crops of Jiangsu, Yangzhou University, Yangzhou 225009, Jiangsu Province, PR China

ARTICLE INFO

Keywords:
Sb_2WO_6
VOCs
Cooked rice
Gas sensor
Density functional theory

ABSTRACT

The palatability of cooked rice is susceptible to the flavor and effective detection of volatile organic compounds (VOCs) can avoid deterioration and improve the taste quality. Herein, hierarchical antimony tungstate (Sb_2WO_6) microspheres are synthesized through a solvothermal process and the effect of solvothermal temperature on the room temperature gas-sensing properties of gas sensors is investigated. Outstanding sensitivity towards VOC biomarkers (nonanal, 1-octanol, geranyl acetone and 2-pentylfuran) in cooked rice is achieved and the sensors exhibit remarkable stability and reproducibility, which are contributed to the formation of the hierarchical microsphere structure, larger specific surface area, narrower band gap and increased oxygen vacancy content. The kinetic parameters combined with principal component analysis (PCA) effectively distinguish the four VOCs while the enhanced sensing mechanism was substantiated through density functional theory (DFT) calculation. This work provides a strategy for fabricating high performance Sb_2WO_6 gas sensors which can be practically applied to food industry.

1. Introduction

As one of the three major grain crops, rice (*Oryza sativa L.*) is planted on 150 million hectares around the world, with a total yield of 600 million tons each year, amounting to 25% of the whole grains (Liu, Zhang, Xu, & Liu, 2021). Using proper cooking methods, rice can be made into different types of staple foods, among which cooked rice is rich in protein, carbohydrates, various minerals and vitamins, etc., making it an essential food on people's tables (Yu, Turner, Fitzgerald, Stokes, & Witt, 2017; Zheng, Zhang, Liu, & Liu, 2022). With the improvement of people's life quality, the taste quality of cooked rice has attracted much more attention. Specifically, taste quality refers to the comprehensive characteristics (appearance, smell, taste, hardness and viscosity) of cooked rice, as the variety of rice, cooking methods and storage conditions will affect the taste quality simultaneously and synergistically. Among numerous evaluation criteria, the flavor of cooked rice has received extensive attention from many researchers, as it exerts a crucial impact on the acceptability of cooked rice for consumers (Yau, & Liu, 1999; Shen, Jin, Xiao, Lu, & Bao, 2009). For more than 300 VOCs generated through Maillard-derived and thermal reactions from cooked rice (Bösl, Dunkel, & Hofmann, 2021), aldehydes, alcohols, ketones, lipids and heterocyclic compounds are the most abundant (Dias, Hacke, Bergara, Villela, Mariutti, & Bragagnolo, 2021), while these various VOCs endow the cooked rice with distinct flavors. In general, aldehydes and lipids give cooked rice a fruity aroma while alcohols release a floral fragrance mostly, while the odor description of four distinct flavors (nonanal, 1-octanol, geranyl acetone and 2-pentylfuran) in cooked rice are listed in Table S1. Moderate concentrations of nonanal and 1-octanol in cooked rice will give off a subtle fragrance whereas higher concentrations will release an unpleasant fatty flavor. As a product of the oxidation of linoleic acid, 2-pentylfuran owns a characteristic nutty flavor at low concentrations and an unpleasant fishy bean odor at high concentrations in cooked rice. Geranyl acetone with fruit and rose aroma will enhance the cooked rice flavor. Therefore, we expected the higher concentration of geranyl acetone in cooked rice (Zheng, Zhang, Liu, & Liu, 2022; Yu, Turner, Fitzgerald, Stokes, & Witt, 2017). In

* Corresponding author.
E-mail address: zhangc@yzu.edu.cn (C. Zhang).

https://doi.org/10.1016/j.foodchem.2023.136323
Received 18 December 2022; Received in revised form 2 May 2023; Accepted 4 May 2023
Available online 9 May 2023

addition, since the sensory evaluation of cooked rice odor is highly subjective and the olfactory sensitivity of the evaluators is quite different, many new evaluating technologies have been developed (Dias, Hacke, Bergara, Villela, Mariutti, & Bragagnolo, 2021; Utz et al., 2022). Therefore, as the VOCs volatilized from cooked rice are affected by multiple factors, studying the changes in VOCs content in cooked rice systematically is crucial for food security and taste quality improvement.

Based on low cost, real-time operability, high response, fine stability and ease of use, semiconductor metal oxides (SMOX), such as CuO, SnO_2 and $ZnSnO_3$, are exploited for VOCs detection in various domestic and industrial applications (Qiao et al., 2018; Choi et al., 2019). Among the many kinds of SMOX, Sb_2WO_6 is the simplest form of the Aurivillius family $(Sb_2O_2)(A_{m-1}B_mO_{3m+1})$ with m = 1 (Zhang, & Chen, 2016), and as a *n*-type semiconductor material with appropriate band gap structure, it is extensively applied in photocatalysis field due to its mighty visible-light acquisition capability (Zhang et al., 2022; Rafiq, Mehraj, Lone, Wahid, & Majid, 2020; Wang et al., 2020), but not much in gas sensors. In detail, Ren et al. prepared Sb_2WO_6/g-C_3N_4 nanocomposite using an ultrasound-assisted method for low-concentration NO removal (Ren, Li, Wu, Wang, & Zhang, 2021). 3D graphene aerogel Sb_2WO_6 hybrid was synthesized by Ding et al. with a facile solvothermal process, as the change of methyl orange concentration under different wavelengths of light irradiation was monitored and the photocatalytic activity of the 3D graphene aerogels Sb_2WO_6 (3DGA/Sb_2WO_6) hybrid was deliberated in detail. Chen et al synthesized Ag-loaded Sb_2WO_6 microspheres through a solvothermal method, and the corresponding photocatalysts were evaluated in degradations of Methyl orange, Rhodamine B and other dye aqueous solution under UV light and visible light irradiation (Ding et al., 2018). In brief, most researchers adopt doping and loading to change the properties of Sb_2WO_6 for improving photocatalytic performance. Table S2 summarizes the current preparation methods and applications for Sb_2WO_6-based materials.

In our previous study, Sb_2WO_6 gas sensors based on pH control were fabricated, which possessed a certain potential for nonanal detection and evaluation of the freshness of cooked rice (Zheng, Liu, Xu, & Zhang, 2022). Specifically, one problem of Sb_2WO_6 gas sensor is to detect macromolecular VOCs under overhigh working temperatures, which may lead to the decomposition of VOC molecules and affect the service life of the gas-sensing material, further weakening the gas sensing performance. Therefore, our present work remains the testing condition at room temperature (25 ± 2 °C). Furthermore, due to the characteristics of a large variety and low concentration of VOCs volatilized from cooked rice, the reported SMOX-based gas sensors suffer from the cross-selectivity and low sensitivity to analytes. To our best knowledge, no studies were implemented for the preparation of Sb_2WO_6 crystals at different reaction temperatures.

Herein, the three-dimensional (3D) hierarchical Sb_2WO_6 microspheres constituted of $\{Sb_2O_2\}^{2n+}$and $\{WO_4\}^{2n-}$ with broad specific surface area, numerous active adsorption sites and superior modified crystal structures are prepared by a facile, one-step solvothermal synthesis. From field emission scanning electron microscopy (FESEM) studies, Atomic Force Microscope (AFM) analysis and high-resolution transmission electron microscopy (HRTEM) consequences, all the samples possess controlled size and shaped particles. Moreover, the relations between the material properties (phase composition, chemical states of elements, thermal stability and optical properties) and composing conditions were anatomized employing X-ray diffraction (XRD), Fourier transform infrared (FTIR) spectroscopy, ultraviolet (UV) spectrum, Raman, photoluminescence (PL), X-ray photoelectron spectroscopy (XPS), thermogravimetric analysis (TGA), specific surface determination (BET) and electron paramagnetic resonance (EPR), which is the first to deliberate the influences of the critical solvothermal synthesis parameters, owning a great deal of significance. The as-prepared optimal Sb_2WO_6 gas sensors had a maximum response of 31.25, 57.75, 11.44 and 12.76 toward 15 ppm nonanal, 1-octanol, geranyl acetone and 2-pentylfuran at room temperature, respectively. In addition, by analyzing the kinetic parameters in the sensing process, the gas sensors combined with PCA are employed for distinguishing the four VOCs in a dataset. Moreover, density functional theory (DFT) calculations were implemented to elaborate the strengthened sensing mechanism. This facile strategy with high efficiency will help the design of SMOX room-temperature gas sensors.

2. Material and methods

All chemicals applied in this work were analytical grade (AR) and directly used without any further purification. $Na_2WO_4{\cdot}2H_2O$ (99.5%) was acquired from Sinopharm Chemical Reagent Co., Ltd. $SbCl_3$ (99%), NaOH (96%) and anhydrous alcohol was obtained from Aladdin Biochemical Technology Co., Ltd. of China.

2.1. Synthesis of hierarchical Sb_2WO_6 microspheres

The hierarchical Sb_2WO_6 microspheres were obtained via a facile one-step solvothermal manner which was modified from our previous studies (Fig. S1) (Zheng, Liu, Xu, & Zhang, 2022). In the concrete synthesis, 16 mmol $SbCl_3$ was dissolved in 32 mL ethanol as an antimony source to form solution A and solution B was formed by dissolving 8 mmol $Na_2WO_4{\cdot}2H_2O$ as tungsten source in 32 mL deionized water. After sufficient stirring, the transparent solutions A and B were mixed to form solution C which contained light yellow flocculent precipitation. 3 mL NaOH solution (20 wt%) was added to solution C drop by drop to form a uniform suspension. In the next step, to obtain the microspheres, the final solution (65 mL) was transferred into a Teflon (Poly tetra fluoroethylene, PTFE) lined solvothermal unit (100 mL) after fully stirring and sonicating for 10 min, on which was subsequently kept at 120 °C to 200 °C with the interval of 10 °C centigrade during 24 h, respectively. Since naturally cooled down to ambient temperature, the sediments were washed with deionized water and absolute ethanol several times in turn, and then dried at 70 °C for 20 h. The as-prepared samples solvothermal treated at120°C, 130 °C, 140 °C, 150 °C, 160 °C, 170 °C, 180 °C, 190 °C and 200 °C were named as SW12, SW13, SW14 SW15, SW16, SW17, SW18, SW19 and SW20, respectively.

2.2. Characterization

The phase structure of nine powders was investigated by XRD (D8 Advance Bruker) using Cu-Kα radiation and micro-Raman spectroscopy (MRS, In via, Renishaw). The morphological characteristics and nanostructure details were determined via FESEM (S4800II Hitachi), HRTEM (Tecnai G2 F30 S-TWIN) and AFM (SPM-9700HT). The surface elements states were analyzed using XPS (Thermo Fisher Scientific ESCALAB 250Xi) while the BET results and the corresponding pore size distributions were calculated (Autosorb IQ3, Quantachrome Instruments). For improving the gas sorption kinetics, 0.15 g of the as-precipitated samples was degassed under vacuum at 200 °C for 10 h before the testing. TGA was carried out under an N_2 atmosphere with a heating rate of 10 °C/min to measure the thermal stability of the as-prepared samples (Pyris 1, Perkin-Elmer, USA). The UV–Vis absorption spectra (200–800 nm) were obtained by the Cary 5000 spectrometer. FTIR spectra were performed on an Agilent 660-IR spectrometer, using the top mount diffuse attachment (*gem* attachment). The oxygen vacancies on the sample surface were investigated via EPR (A300-10/12, Bruker) and a laser confocal Raman spectrometer (Renishaw inVia).

2.3. Gas sensing setup

To manufacture the gas sensors, the target solutions were obtained by mixing Sb_2WO_6 powders (~3 mg) with deionized water (~1 mL) uniformly, then drop coated onto the Al_2O_3 substrate equipped with interdigital Pt electrodes which adopt coplanar design and passivated, thus obtaining highly thermal stability. After being aged at 120 °C for

24 h for stability enhancement, the Sb_2WO_6 sensors were obtained. The room temperature (25 ± 2 °C) gas sensors testing system is displayed in Fig. S2 and more testing information has been added in Supplement materials. Through the homemade testing equipment, resistance signals are obtained for further analysis. In detail, the response (*n*-type) is defined as Ra/Rg (Ra and Rg represent the steady resistance values in pure air and target VOC, respectively) and response/recovery time represents the duration required to reach a 90% change of resistance in a full sensing behavior of response/recovery processing.

3. Results and discussion

3.1. Structural and morphological characteristics

The results of the phase and crystal structure of synthesized Sb_2WO_6 samples were taken with XRD studies (Fig. S3a). The phase of the samples altered slightly while the XRD patterns were in good accordance with Sb_2WO_6 in the triclinic phase (JCPDS # 47–1680) approximately (Yang, Yang, Li, Li, & Cao, 2016) and each characteristic peak is sharp, indicating the good crystallinity and high purity. The typical peaks of Sb_2WO_6 were calculated using gaussian fitting occurred at 20.389°, 26.825°, 29.290°, 32.753°, 36.327°, 40.169°, 47.360°, 49.788°, 53.209° and 55.410°, corresponding to (01–1), (1–11), (003), (20–1), (020), (202), (023), (-2–21), (310) and (311) planes (Ding et al., 2018). With the increase of solvothermal temperature, the peak position does not shift obviously, but the peak shape slightly changes from a diffuse long peak to a blunt peak with a smaller half-height and width, which indicates that the overall structure of Sb_2WO_6 microspheres becomes more compact with the increase of solvothermal temperature (Zhang, Li, Chen, Xiang, Hu, & Li, 2021).

In order to further explore the Sb_2WO_6, some physical properties (d-spacing value (Å), crystallite size, lattice parameter, FWHM and lattice strain) of the synthesized Sb_2WO_6 microspheres obtained by XRD pattern are represented in Table S3. Specifically, the crystallite sizes, d-spacing value and the lattice strain of samples can be calculated by Scherrer formula (Equation (1), Bragg formula (Equation (2) (Meng, Li, Fu, & Fu, 2015) and Equation (3) (Zhang, Li, Chen, Xiang, Hu, & Li, 2021), respectively. In detail, the most intense peak at 26.824° was selected to obtain the crystallite size of all samples.

$$D = \frac{k\lambda}{\beta\cos v} \tag{1}$$

$$2d\sin\theta = n\lambda \tag{2}$$

$$Lattice\ strain = \frac{\beta\cos v}{\lambda} \tag{3}$$

Where *v* is Bragg angle of the strongest peak corresponding to (1–11) plane in degrees and β is its corresponding FWHM (in radians) while the degree forms can be obtained by multi-peaks Gaussian fitting. *k* represents the shape factor of 0.9 and λ is the wavelength of X-ray source ($CuK_\alpha = 0.15406$ nm). *n* is the diffraction order, for the first-order $n = 1$, while *d* is the interplanar spacing in Å. As synthesized Sb_2WO_6 pertains to the triclinic system, the lattice constant (a, b and c) can be obtained by homologous calculation formula (Equation (4)–(6) (Vermeulen, Kube, & Norberg, 2019).

$$\frac{1}{d^2} = \frac{1}{a^2b^2c^2(1-\cos^2\alpha-\cos^2\beta-\cos^2\gamma+2\cos\alpha\cos\beta\cos\gamma)}(S_1+S_2) \tag{4}$$

$$S_1 = b^2c^2\sin^2\alpha h^2 + a^2c^2\sin^2\beta k^2 + a^2b^2\sin^2\gamma l^2 \tag{5}$$

$$\begin{aligned} S_2 =& 2abc^2(\cos\alpha\cos\beta-\cos\gamma)hk + 2ab^2c(\cos\gamma\cos\alpha-\cos\beta)lh \\ &+ 2a^2bc(\cos\beta\cos\gamma-\cos\alpha)kl \end{aligned} \tag{6}$$

The chemical composition and valence state was evaluated via in situ XPS as depicted in Fig. S3b and Fig. S4. As revealed in Fig. S3b, all the as-prepared samples contained the corresponding elements including Sb, W, O and C with no other elements. As the use of carbon tape for energy calibration, the C 1s peak is shown at 284.8 eV. As shown in Fig. S3b, the overlapped low-resolution XPS spectrum of Sb $3d_{5/2}$ and O 1s can be observed. Two binding energies at 539.91, 539.89, 539.85, 539.76, 539.54, 539. 74, 539.44, 539.83, 539.57 eV and 530.58, 530.59, 530.54, 530.47, 530.23, 530.43, 530.18, 530.48, 530.23 eV in SW12-SW20 spectra assigned to Sb $3d_{3/2}$ and Sb $3d_{5/2}$ with the oxidation state of Sb^{3+} apart (Ding et al., 2018) are shown in Fig. S4a. Take SW16 and SW18 as examples in Fig. S4b, the W 4f spectra of Sb_2WO_6 can be divided into four peaks locating at 37.65 eV, 35.77 eV, 35.33 eV, 34.13 eV and 37.48 eV, 35.62 eV, 35.21 eV, 34.11 eV, respectively, delegating W^{6+} $4f_{5/2}$, W^{5+} $4f_{5/2}$, W^{6+} $4f_{7/2}$ and W^{5+} $4f_{7/2}$ separately. Fig. S4c reveals the detailed spectra of O 1s in all samples. The peaks of SW18 situated at 530.86, 530.16 and 529.81 eV corresponded to chemisorbed oxygen species (O_C), oxygen vacancy (O_V) and lattice oxygen (O_L), respectively. As the oxygen content (O_C and O_V) in SW18 applied the biggest proportion, which was beneficial to the VOCs sensing performance (Liu, Zheng, Debliquy, & Zhang, 2022). The detailed information on oxygen peaks for all as-prepared samples was shown in Table S4. It is worth noting that, as the solvothermal temperature rises, the peaks of Sb, O, and W of SW12 to SW17 samples show blueshifts, which is due to the chemical bond between Sb with O and the lower electronegativity of Sb. As the solvothermal temperature still rises, the peaks of SW18-SW20 show redshifts specifically, as the binding energy gets smaller and the electron cloud density increases, enhancing the Sb_2WO_6 to lose electrons and generate more oxygen species (O_2^-, O^- and O^{2-}) (Wang et al., 2021). In the actual gas sensing process, when VOCs molecules contact with more oxygen molecules, more quantity of electrons will transfer back to Sb_2WO_6, thus the resistance signals will decline swiftly, improving the sensitivity to the target gas.

The morphology and microstructure of the nine samples were investigated via FESEM, HRTEM and AFM. Fig. S5 and Fig. S6 depicted the typical FESEM images of all samples and EDS results of SW18. All samples consist of a large amount of thin interconnected nanosheets and nanowires which assemble the corresponding microspheres with a diameter of 3–5 μm. In detail, from the morphology of SW12 to SW15, the self-assembled Sb_2WO_6 microspheres can be observed, on which a great number of nanosheets and nanowires aggregated are dispersed separately, which can also be described as sea urchin-like microspheres. As the solvothermal temperature continues to rise, the microspheres of SW16 to SW20 are relatively compact, while the nanosheets and nanowires are closely embedded together, indicating that the rise of solvothermal temperature intensifies the rate and degree of nucleation. From the low-magnification SEM photos as shown in Fig. S5a-S5b, some of the SW16 and SW18 microspheres are single-dispersed, while others are glued together to form some aggregations. As shown in Fig. S5c-S5f, it can also be confirmed that the rise of solvothermal temperature would increase the tightness of the Sb_2WO_6 microsphere from the high-magnification SEM images of the two representative morphologies (SW16 and SW18). From the EDS results of SW18, the primary elements are Sb, W, O, and their proportions are in line with the stoichiometric ratio of Sb_2WO_6 materials (Fig. S6o). The nanowires and nanosheets over SW18 hierarchical microspheres are more distinct and with consistent order, which can provide more sites for oxygen species and VOC adsorption. Appropriate morphology conduces to the broadening of interface contact area between VOCs and sensing material, which may benefit the separation of space charges and more charge carriers are capable to migrate to the material surface for participating gas sensing process. In addition, according to the AFM images (Fig. S7), the thickness of the SW18 microspheres deposited on the gas sensors is about 400 nm, of which the nanosheet is around 20–40 nm.

Fig. S5g illustrates the growth mechanism of Sb_2WO_6 microspheres, which comprised five steps including the nucleation process, anisotropic growth, self-assembling, directional attachment growth, and ulteriorly crystallization (Yang, Yang, Li, Li, & Cao, 2016). Firstly, the tiny crystal

nuclei grow along the plane direction of the crystal in the saturated solution. Due to the anisotropy of the crystal, the nanosheet structure of Sb_2WO_6 is formed. Since the existence of energy differences among particles, the larger Sb_2WO_6 particles will engulf the smaller Sb_2WO_6 particles to further grow. From the perspective of thermodynamics, individual nanosheets tend to grow vertically on the surface of microspheres for reducing surface energy. As a result, the nanosheets and nanowires of precursor incline to stick to each other and self-assemble to take shape of the spherical crystals. Specifically, the hydrogen and electrostatic bonds in the ethanol and water mixed solution allow the nanosheets and nanowires to grow along the common crystal orientation. Finally, as the solvothermal time increases, regular hierarchical Sb_2WO_6 microspheres eventually form after further crystallization.

Fig. 1a-1c shows the TEM images of SW18, which further confirms the formation of the hierarchical microspheres. The selected area electron diffraction (SAED) pattern of SW18 in Fig. 1d displays that the interplanar spacing of the four diffraction rings indexed to the (1–11), (003), (020) and (023) lattice plane of the triclinic Sb_2WO_6 microspheres, respectively. In Fig. 1e-1f, an HRTEM image obtained from a portion of a single Sb_2WO_6 polycrystalline nanocrystal is shown, which indicates the polycrystalline nature of as-synthesized Sb_2WO_6 samples. The image shows a clear lattice fringe domain with an interplanar spacing of about 0.32 nm, 0.28 nm and 0.26 nm, consistent with the (1–11), (123) and (023) plane from triclinic Sb_2WO_6 structure accordingly, which is also identical with the XRD calculation results in Table S3. Fig. 1g-1j demonstrates the EDS element maps of the single hierarchical Sb_2WO_6 microspheres. The relative uniform distribution of Sb, W and O on the whole microsphere can be observed, while there are some dark shadows at the bottom of the O mapping, which is due to the solid microsphere with too large particle size.

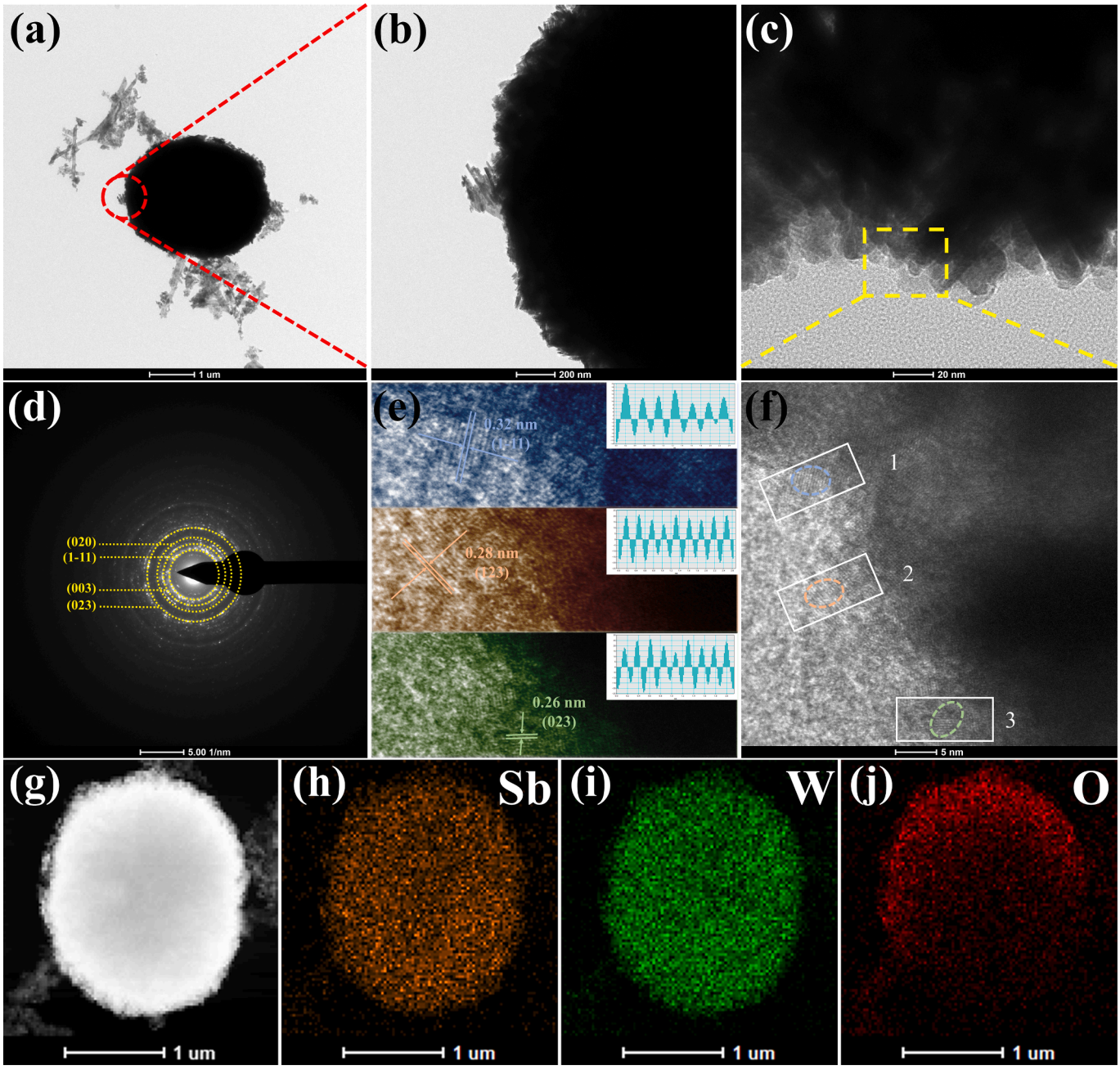

Fig. 1. Microstructure details of SW18: (a, b, c) HR-TEM images; (d) SAED pattern; (e-f) lattice distance of various crystal planes (inset: intensity profiles of Sb_2WO_6 in the marked area 1, 2 and 3 in panel f); (g) HAADF image and (h-j) the corresponding elemental mapping of Sb, W, O, and their overlapping images, respectively.

Firstly, the FT-IR and UV–vis analysis were given in Supplementary materials. Then, to probe into the increasing oxygen vacancies generated during the solvothermal process, EPR technique was utilized to characterize the unpaired electrons in the Sb_2WO_6. From the spectra of SW14 and SW18 (Fig. 2d), signals occurred at g = 2.003 corresponding to the point where electrons were seized by the oxygen vacancies. Both two samples possessed certain amounts of oxygen vacancies and a stronger signal was detected in SW18. Numerous oxygen vacancies appear on the surface or inside of the crystal structure of SW18 sample, which can act as active sites during the gas catalysis process, significantly shortening the response time and strengthen the VOC response (Qin, Yuan, Shen, Zhang, & Meng, 2022).

Fig. 2e shows the PL spectra of SW14 and SW18 and the peaks appear in both samples. The emission peak at 500 nm to 650 nm is mainly caused by the presence of oxygen vacancy. When more contents of oxygen vacancies exist in Sb_2WO_6, the energy required for electron transition decreases, thus the energy released when photogenerated electrons and holes recombined is relatively low. The visible light with a wavelength between 500 nm and 650 nm can trigger the photoluminescence phenomenon of Sb_2WO_6, while the intensity of SW18 luminescence peak is the largest, indicating the existence of oxygen vacancies (Rafiq, Mehraj, Lone, Wahid, & Majid, 2020). Thus, the appropriate solvothermal temperature (180 °C) should be selected to obtain the sample with the oxygen vacancy of the highest concentration. The BET and TGA analysis were given in Supplementary materials.

3.2. Gas sensing performance

To study the impact of solvothermal temperature regulating on the VOCs sensing performance of Sb_2WO_6, the gas sensing test was carried out based on the sensors manufactured with Sb_2WO_6 samples, in which 1-octanol, 2-pentylfuran geranyl acetone and nonanal were selected as target VOCs. All the operating temperatures in the sensing testing are set at room temperature (25 ± 2 °C).

The sensors' dynamic responses to different concentrations (3 ~ 15 ppm) of 1-octanol, 2-pentylfuran geranyl acetone and nonanal are depicted in Fig. 3. The response of all gas sensors is viewed as a reversible transient of its resistance when it comes in contact with or leaves the VOCs. For all the sensors, the response increased with injecting more VOCs. With the lowest concentration of VOCs, SW14 gas sensor exhibited responses of 2.28 and 32.96 for 3 and 15 ppm 1-octanol, respectively, whereas the SW18 gas sensor demonstrated significant improvements, reaching values of 3.44 and 57.75 for 3 and 15 ppm, respectively. As for other VOCs, the response values of the SW12 to SW20 gas sensors when exposed to different concentrations of VOCs at room temperature are listed in Table S6.

The gas response value of each sensor is presented in the configuration of dot plot with error bar (n = 3) (Fig. S10), and the SW18 sensor showed higher responses than other sensors for nonanal, 1-octanol, geranyl acetone and 2-pentylfuran. In addition, the response of the sensor versus the concentration of VOCs vapor was used for linearity evaluation. The details were given in the Supplementary materials. The correlation factor (R^2) of SW18 sensor to 1-octanol, 2-pentylfuran, geranyl acetone and nonanal reaches 0.98685, 0.99699, 0.99003 and 0.99408, respectively, indicating the excellent linear fitting and high reliability in practical applications (Fig. S11). Furthermore, the LOD of the SW18 sensor for 1-octanol, 2-pentylfuran, geranyl acetone and nonanal can be estimated to be 943 ppb, 843 ppb, 821 ppb and 1042 ppb, individually. The results indicated the Sb_2WO_6 based gas sensors own an excellent capacity for detecting ultralow concentration VOCs vapor.

As humidity exerts an important impact on the sensing performance of SMOX gas sensors (Yan et al., 2021), the sensing tests on VOCs under different humidity conditions were carried out. The coefficient of variation (CV) is applied for evaluating the impact of RH on the sensitivity of sensors, which can be obtained from Equation (7) listed in Table S7.

$$CV = S_{SD}/S_a \times 100\% \tag{7}$$

where S_{SD} and S_a are the standard deviation of response values and average response values under different humidity environments, respectively (Yao, Tang, Wang, Nath, & Xu, 2016). A higher CV value means worse anti-interference performance. At 12 ppm nonanal, the CV values of the SW14 and SW18 are 65.58% and 77.89% when changing RH from 20% to 80% as shown in Fig. 4a-4b, indicating the better anti-humidity property of SW14 gas sensor (Fig. 4c).

Fig. 4d shows 14 continuous response-recovery cycles for sensing 9 ppm geranyl acetone, SW18 gas sensor owns the ability to supply almost equal response amplitudes and the response values are maintained at about 6.907, which demonstrates favorable repeatability. As shown in Fig. 4e, the SW18-based sensor towards 15 ppm geranyl acetone demonstrates less than 7% fluctuation in response after 15 days, exhibiting the excellent long-term stability of the as-prepared sensor.

3.3. Gas sensing mechanism and working principle

Triclinic-type Sb_2WO_6 has a *n*-type semiconducting property while the gas-sensing mechanism can be illuminated via the oxygen adsorption theory (Wang et al., 2018). In detail, the fundamental sensing mechanism of Sb_2WO_6 gas sensors can be described by a course of oxygen adsorption in the oxygenated anionic species (O_2^-, O^-, O^{2-}) onto the surface of Sb_2WO_6 and the interaction between adsorbed oxygens with VOCs molecules (Grossmann, Pavelko, Barsan, & Weimar, 2012; Fort, Mugnaini, Pasquini, Rocchi, & Vignoli, 2011). As shown in Fig. 5d, when the as-prepared sensor is exposed to pure air at around 25 °C, chemisorbed oxygen species (O_2^-) will generate from absorbed oxygen on the surface of Sb_2WO_6, as shown with Equations (8)–(11) (Zhou, Zeng, Chen, Xu, Kumar, & Umar, 2019; Li, Zhou, Peng, & Liao, 2020). When VOCs vapor was injected into the chamber and reacted with the O_2^-, the electrons will migrate and be transferred to the conduction band of Sb_2WO_6. Then the electron depletion layer will shrink and with the increase in resistivity (Equation (12)–(15)). Besides oxygen, water molecules could also cause chemisorption, leading to competition with the target gas for adsorption sites in most cases, further reducing the sensitivity of gas sensors (Wang et al., 2022).

$$O_2(gas) \leftrightarrow O_2(ads) \tag{8}$$

$$O_2(ads) + e^- \leftrightarrow O_2^-(ads)(T < 150^\circ C) \tag{9}$$

$$O_2^-(ads) + e^- \leftrightarrow 2O^-(ads)(150^\circ C < T < 400^\circ C) \tag{10}$$

$$O^-(ads) + e^- \leftrightarrow O^{2-}(ads)(T > 400^\circ C) \tag{11}$$

$$C_9H_{18}O_{(gas)} + 13O_2^- \rightarrow 9CO_{2(gas)} + 9H_2O + 13e^- \tag{12}$$

$$C_8H_{18}O_{(gas)} + 12O_2^- \rightarrow 8CO_{2(gas)} + 9H_2O + 12e^- \tag{13}$$

$$C_{13}H_{22}O_{(gas)} + 18O_2^- \rightarrow 13CO_{2(gas)} + 11H_2O + 18e^- \tag{14}$$

$$C_9H_{14}O_{(gas)} + 12O_2^- \rightarrow 9CO_{2(gas)} + 7H_2O + 12e^- \tag{15}$$

To explore the enhanced sensing mechanism further, the conduction band potential (E_{CB}) of the samples is calculated below and the valence band potential can be obtained by VB-XPS technique (Fig. 5a). The $E_{VB, XPS}$ of SW14 and SW18 is measured to be 1.67 and 1.48 eV, respectively.

$$E_{VB,\ NHE} = \varphi + E_{VB,\ XPS} - 4.44 \tag{16}$$

where φ is the work function of the instrument (4.52 eV) and $E_{VB, XPS}$ refers to the valence band potential. Therefore, the standard hydrogen electrode for the valence band potential ($E_{VB, NHE}$) of SW14 and SW18 is calculated to be 1.75 and 1.56 eV by Equation (17). Furthermore, the work function in actual VOCs detection (Φ) and the contact potential

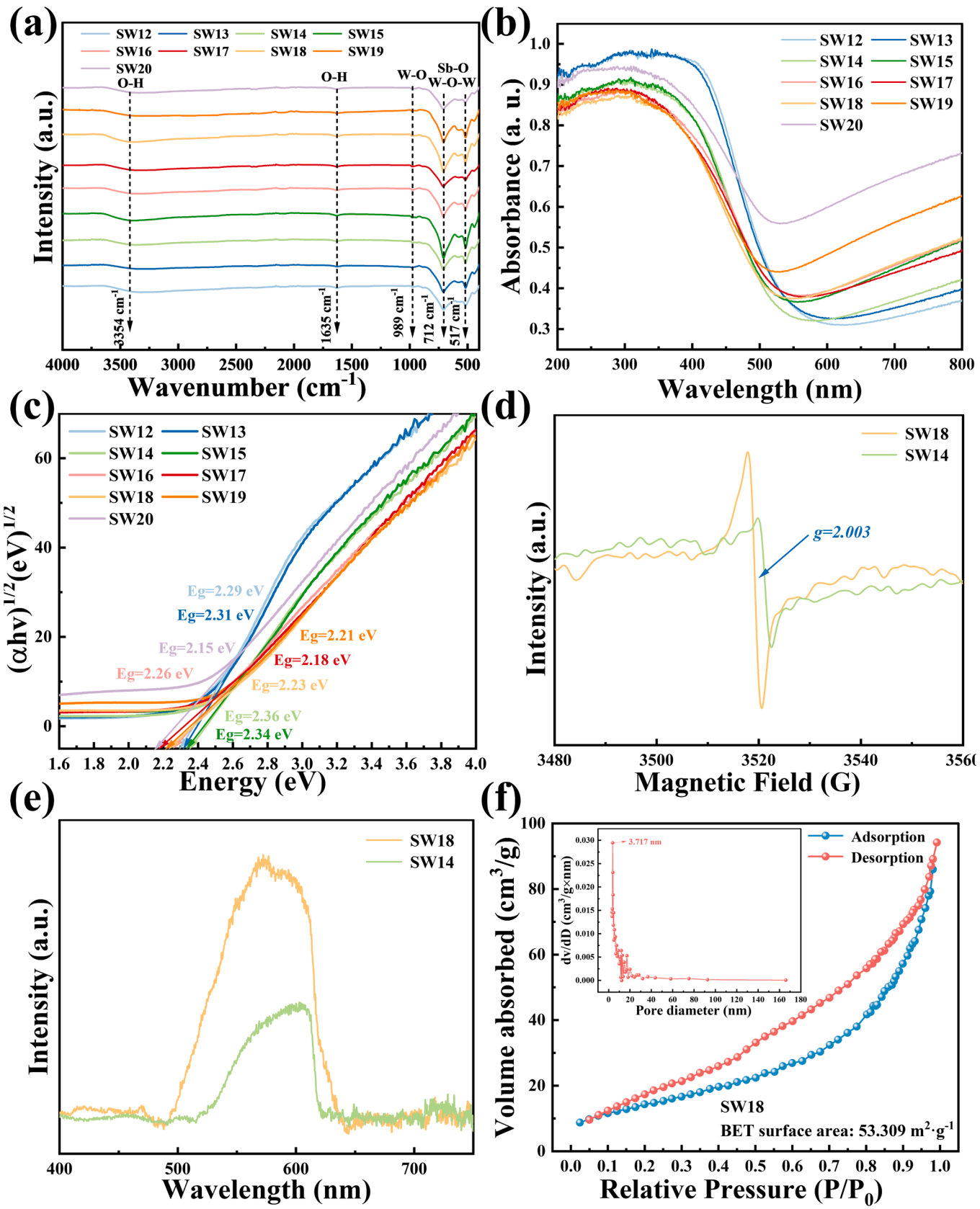

Fig. 2. (a) FTIR spectra of all Sb_2WO_6 samples; (b) UV–Vis diffuse absorbance spectra of all Sb_2WO_6 samples; (c) The calculated band gap energies of all Sb_2WO_6 samples; (d) EPR spectra of SW14 and SW18; (e) Raman spectra of SW14 and SW18; (f) N_2 adsorption–desorption isotherms (inset: pore-size distribution) of SW18.

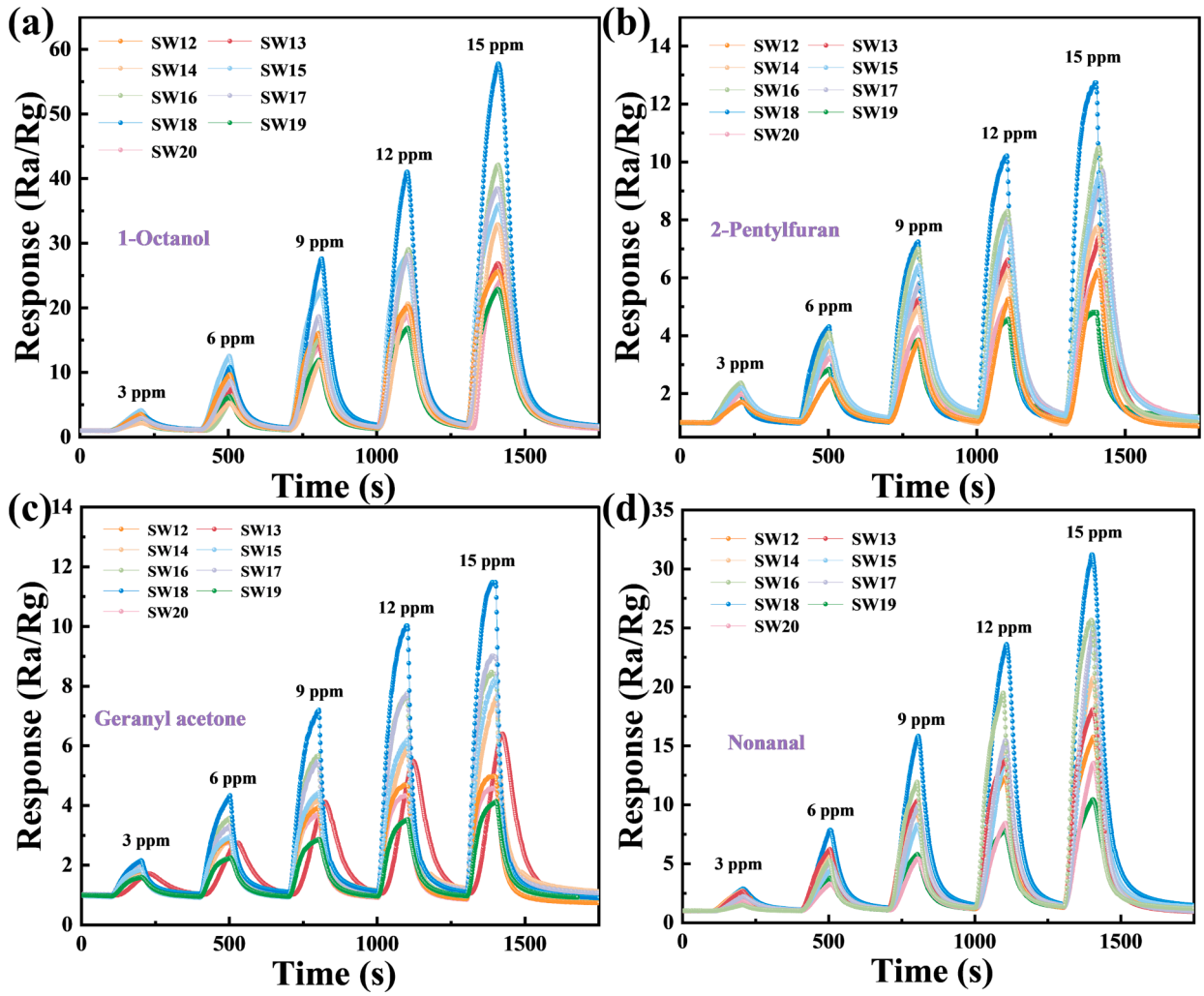

Fig. 3. Dynamic response curves of the nine as-prepared gas sensors (SW12-SW20) exposed to different concentrations of (a) 1-octanol; (b) 2-pentylfuran; (c) geranyl acetone and (d) nonanal at room temperature.

difference (ΔV) own the relationship below (Li et al., 2021):

$$\Delta V = \Phi - \varphi \tag{17}$$

The distance between the two inflection points (IP) of the plot is defined as ΔV (Fig. 5b-5c). Thus, the Φ of SW14 and SW18 is 6.21 eV and 6.84 eV, respectively, then the band structure can be obtained (Fig. 5f). Combined with all characterization assays and gas sensitivity tests, by adjusting the solvothermal temperature during the preparation of Sb_2WO_6, oxygen vacancies are regulated and the band structure of metal oxide materials is changed. Compared SW18 with SW14, as the oxygen vacancy concentration is increased, the resulting free electrons will form a new donor energy level in the forbidden band. Then hybridization occurs when the new donor level is in contact with the valence band, and the top of the valence band expands and shifts upward, narrowing the band gap (Wang et al., 2012). Furthermore, the increase of solvothermal temperature magnifies the Fermi level by 0.63 eV, indicating the enhancement of charge carrier compensation from the formation of the nanosheets heterojunction, which results in better VOCs sensing performance.

Combining the characterization results of FETEM and HRTEM, as a hierarchical nanostructure, Sb_2WO_6 microspheres are spontaneously assembled from nanowires and nanosheets into higher-dimensional matrix structures (micron level) with periodic pores, which maximize gas accessibility without sacrificing electron depletion near the surface of nano-building units. For some specific materials with distinct pore radius (less than100 nm), as a molecule is more susceptible to collide with pore walls than with other gas/vapor molecules, the free passage of vapor molecules is primarily dominated by pore walls rather than the molecules nearby. Therefore, the Knudsen diffusion phenomenon can be used to describe the VOC's transport without external pressure. The corresponding diffusion coefficient (DK) is displayed in Equation (18).

$$D_K = \frac{4r}{3}\sqrt{\frac{2RT}{\pi M}} \tag{18}$$

where M refers to the molecular weight, r is the pore radius, T is the operation temperature (25 °C) and R is the universal gas constant (8.314 J/(mol*K)) (Nandi, Nag, Saha, & Majumdar, 2018). In detail, the molecular weight of 1-octanol, 2-pentylfuran, geranyl acetone and nonanal is 130.23, 138.21, 194.32 and 142.24, respectively and the average pore radius of as-prepared samples can be obtained from BET results (Table S5). The diffusion coefficients of 4 VOCs molecules for all samples were listed in Table S8, while the SW18 possessed the highest diffusion coefficient value, which is consistent with the best gas sensing performance of SW18 sensors.

As 300 VOCs released in cooked rice, the Eley-Rideal model is used to explore the kinetic characteristics in the process of VOCs sensing, while the calculated parameters can be further used to distinguish different VOCs (Šetkus, 2002). The specific calculations were given in the Supplementary materials. To distinguish the four detected VOCs intuitively, the above information in Table S11 was employed as a dataset (4 × 4

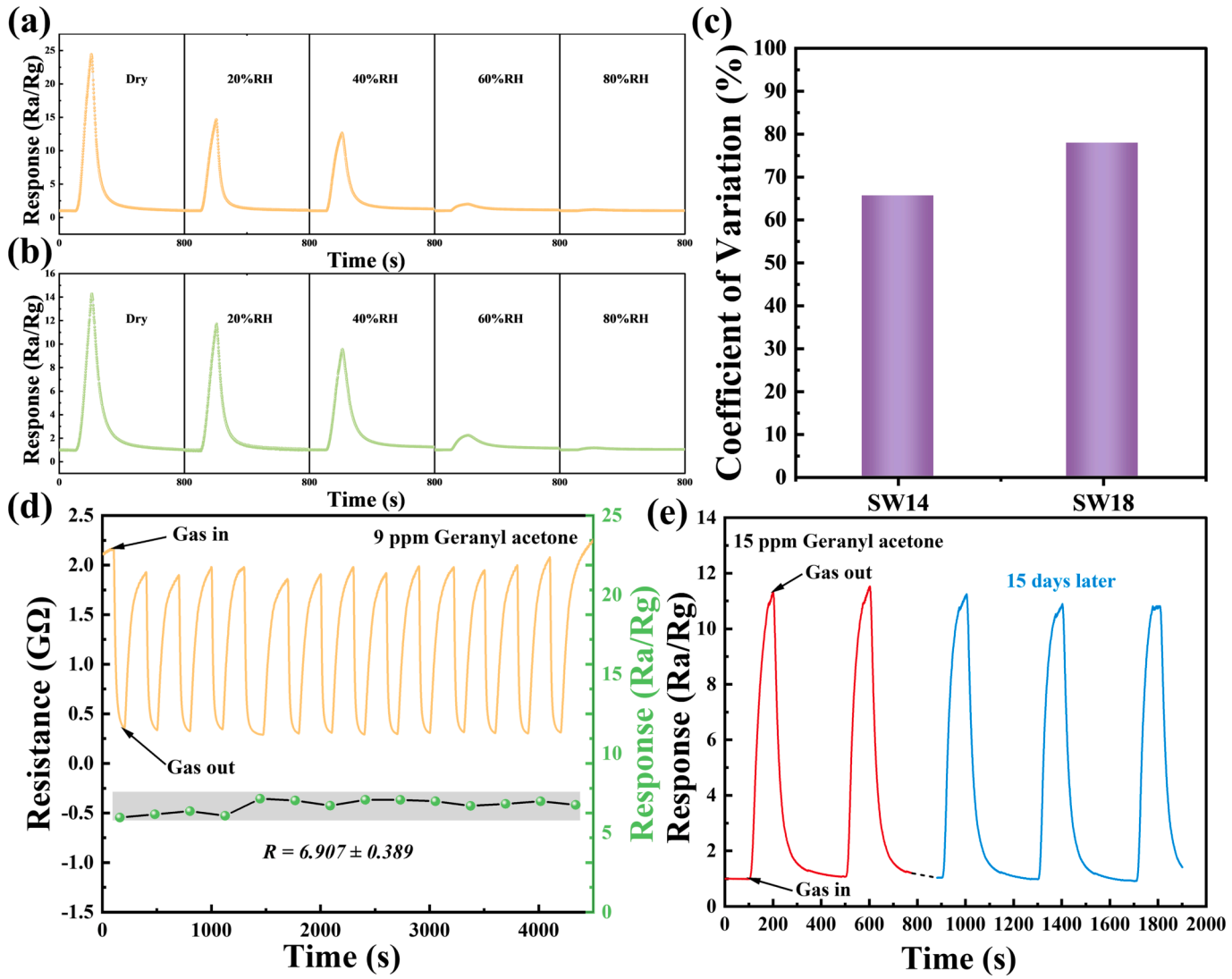

Fig. 4. (a-b) The responses of SW14 and SW18 gas sensors to 12 ppm nonanal under different relative humidity (0%-80%); (c) CV of the sensors by varying RH from 0% to 80% (nonanal 12 ppm, 25 °C); (d) The characterization of short-term stability of SW18-based sensor under 9 ppm geranyl acetone for 14 cycles; (e) The characterization of long-term stability for SW18-based sensor under 15 ppm geranyl acetone testing condition.

matrix) to acquire a scatter plot by dimensionality reduction (Murthy et al., 2015). Specifically, the four kinetic parameters (sensitivity, kinetic reaction rate, β value, and activation energy) were set as input characteristics, while the in-depth differentiation among the VOCs can be achieved by PCA. Herein, the PCA analysis is to display detected VOCs in the common coordinate plane by focusing on the kinetic properties. The target points (1-octanol, 2-pentylfuran, geranyl acetone and nonanal) displayed the isolated location in Fig. 6 distinctly, which supply a facile way for identifying the tested VOCs selectively. Distinguishing the volatile components in cooked rice effectively can modify the data analysis, improve the selectivity of gas sensor and possess a more accurate control of the quality of cooked rice.

To further explore the gas sensing mechanism for the selectivity of four VOCs to Sb_2WO_6, the adsorption behaviors between sensing material surface and VOC molecules (1-octanol, 2-pentylfuran, geranyl acetone and nonanal) were simulated by the CASTEP modules (Material Studio) and other setting details of the DFT calculation are given in the supplementary materials. After surface cleaving of optimal Sb_2WO_6 crystal, the adsorption energy of VOC molecules on Sb_2WO_6 (0 0 1) can be calculated by Equation (19):

$$E_{ads} = E_{total} - (E_{(001)} + E_{VOC}) \quad (19)$$

where E_{total} refers as total energy of VOC molecules absorbed on the certain crystal facet of Sb_2WO_6 surface system, $E_{(0\,0\,1)}$ is the energy towards (0 0 1) Sb_2WO_6 surface, and E_{VOC} refers to the energy of the isolated VOC molecules. The crystal structure of Sb_2WO_6 after geometric optimization and the band structure of Sb_2WO_6 in TRI_{1a} lattice was shown Fig. S13 and Fig. S14, respectively. To obtain the absorption energy, the geometry structure for 1-octanol, 2-pentylfuran, geranyl acetone and nonanal adsorption systems of Sb_2WO_6 are built and depicted in Fig. S15. It follows that the distance between 1-octanol, 2-pentylfuran, geranyl acetone, nonanal molecule and the substrates are 2.707 Å, 3.238 Å, 2.347 Å and 2.405 Å and their adsorption energies on the surface are −2.65 eV, −1.2 eV, −0.95 eV and −2.14 eV, respectively, which are shown at Fig. S16a. The adsorption energy indicating the strongest binding of 1-octanol molecule to Sb_2WO_6 surface among four VOCs, while the stronger adsorption energy reveals the longer recovery time in the sensing test (Geng et al., 2021). In addition, the charge transfer between the adsorbed VOCs and the Sb_2WO_6 gel sensor is proportional to the sensor response value or the sensitivity, which is in coordination with the experimental results (Fig. S16b) (Barsan, Koziej, & Weimar, 2007).

Furthermore, based on the optimized structures of the Sb_2WO_6 (0 0 1)

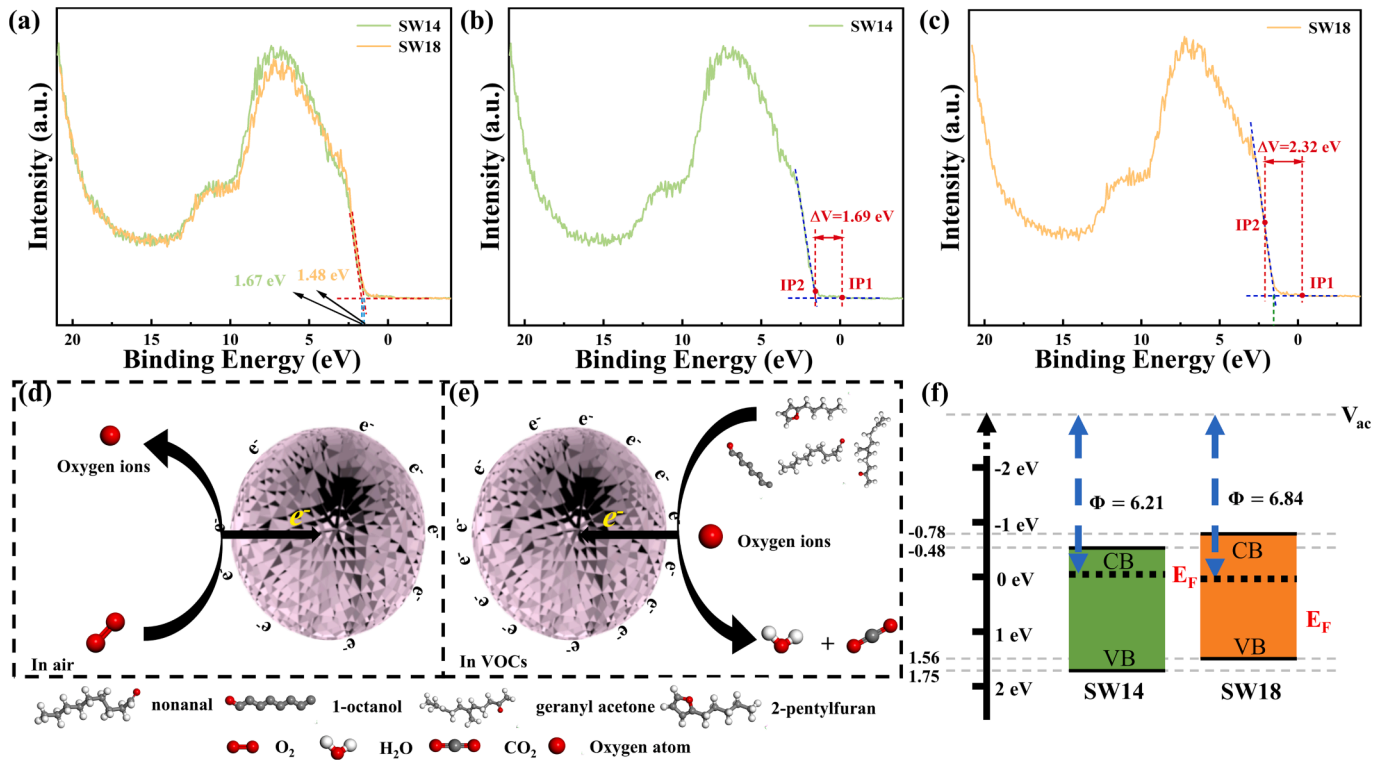

Fig. 5. (a) VB-XPS of SW14 and SW18; Work functions of (b) SW14 and (c) SW18; (d) The schematic illustration of gas-sensing mechanism for Sb_2WO_6; (e) Band structure of SW14 and SW18.

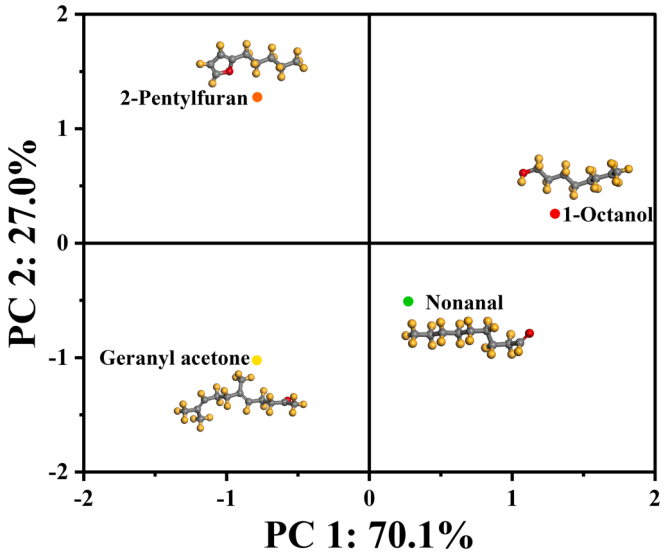

Fig. 6. Scatter plot obtained through PCA performed over gas sensing kinetic parameter results for tested VOCs.

model (Fig. S16a), the density of states (DOS) of Sb_2WO_6 can be calculated as shown in Fig S16(c-f). The valence band maximum of Sb_2WO_6 primarily consists of O 2p orbital and the conduction band minimum of Sb_2WO_6 is the formation of hybrid orbitals of W 5d and O 2s. Therefore, the physicochemical-induced charge carriers are generated from the O 2p orbital of Sb_2WO_6 and can be stimulated via the hybrid orbitals of W 5d and O 2p.

4. Conclusions

In summary, a novel self-assembled hierarchical Sb_2WO_6 microspheres were prepared. Sb_2WO_6 gas sensor fabricated by samples synthesized at 180 °C owns the remarkable sensing performance towards 4 predominant VOCs released from cooked rice, while the average response can reach 57.75, 12.76, 11.44 and 31.25 towards 15 ppm 1-octanol, 2-pentylfuran, geranyl acetone and nonanal, respectively. The enhanced gas sensing performance of the hierarchical Sb_2WO_6 microspheres is mainly contributed to its multi-stage morphology, high specific surface area, abundant oxygen vacancy and narrower band gap, which can provide enough adsorption sites for oxygen and VOCs molecules and accelerate the movement of charge carriers. The above results verified that synthesis temperature controlling can regulate the physicochemical properties of Sb_2WO_6, and further improve the sensing performance of VOCs detection.

CRediT authorship contribution statement

Chao Zhang: Conceptualization, Writing – review & editing, Funding acquisition, Writing – original draft, Supervision. **Zichen Zheng:** Conceptualization, Methodology, Investigation, Formal analysis, Resources. **Kewei Liu:** Investigation, Writing – review & editing. **Marc Debliquy:** Writing – review & editing. **Qiaoquan Liu:** Supervision, Resources.

Declaration of Competing Interest

The authors declare that they have no known competing financial interests or personal relationships that could have appeared to influence the work reported in this paper.

Data availability

Data will be made available on request.

Acknowledgments

This work was supported by the Outstanding Youth Foundation of Jiangsu Province of China (No. BK20211548), the National Natural Science Foundation of China (No. 51872254), the National Key Research and Development Program of China (No. 2017YFE0115900) and the Graduate Research Innovation Program of Jiangsu Province of China.

Appendix A. Supplementary data

Supplementary data to this article can be found online at https://doi.org/10.1016/j.foodchem.2023.136323.

References

Barsan, N., Koziej, D., & Weimar, U. (2007). Metal oxide-based gas sensor research: How to? *Sensors and Actuators B: Chemical, 121*, 18–35. https://doi.org/10.1016/j.snb.2006.09.047

Bösl, M., Dunkel, A., & Hofmann, T. F. (2021). Rapid, High-Throughput Quantitation of Odor-Active 2-Acetyl Azaheterocycles in Food Products by UHPLC–MS/MS. *Journal of Agricultural and Food Chemistry, 69*, 1405–1412. https://doi.org/10.1021/acs.jafc.0c07144

Choi, Y. M., Cho, S.-Y., Jang, D., Koh, H.-J., Choi, J., Kim, C.-H., et al. (2019). Ultrasensitive Detection of VOCs Using a High-Resolution CuO/Cu_2O/Ag Nanopattern Sensor. *Advanced Functional Materials, 29*, 1808319. https://doi.org/10.1002/adfm.201808319

Dias, L. G., Hacke, A., Bergara, S. F., Villela, O. V., Mariutti, L. R. B., & Bragagnolo, N. (2021). Identification of volatiles and odor-active compounds of aromatic rice by OSME analysis and SPME/GC-MS. *Food Research International, 142*, Article 110206. https://doi.org/10.1016/j.foodres.2021.110206

Ding, C. Q., Li, Z. Q., Tan, W. S., Li, H. D., Ma, J. F., Chen, Z. P., et al. (2018). 3D graphene aerogels/Sb_2WO_6 hybrid with enhanced photocatalytic activity under UV- and visible-light irradiation. *Synthetic Metals, 246*, 137–143. https://doi.org/10.1016/j.synthmet.2018.10.010

Fort, A., Mugnaini, M., Pasquini, I., Rocchi, S., & Vignoli, V. (2011). Modeling of the influence of H_2O on metal oxide sensor responses to CO. *Sensors and Actuators B-Chemical, 159*, 82–91. https://doi.org/10.1016/j.snb.2011.06.052

Geng, X., Li, S., Mawella-Vithanage, L., Ma, T., Kilani, M., Wang, B., et al. (2021). Atomically dispersed Pb ionic sites in PbCdSe quantum dot gels enhance room-temperature NO_2 sensing. *Nature Communications, 12*, 4895. https://doi.org/10.1038/s41467-021-25192-4

Grossmann, K., Pavelko, R. G., Barsan, N., & Weimar, U. (2012). Interplay of H-2, water vapor and oxygenat the surface of SnO_2 based gas sensors - An operando investigation utilizing deuterated gases. *Sensors and Actuators B-Chemical, 166*, 787–793. https://doi.org/10.1016/j.snb.2012.03.075

Li, B., Zhou, Q., Peng, S., & Liao, Y. (2020). Recent Advances of SnO_2-Based Sensors for Detecting Volatile Organic Compounds. *Frontiers in Chemistry, 8*, 321. https://doi.org/10.3389/fchem.2020.00321

Li, X., Kang, B., Dong, F., Zhang, Z., Luo, X., Han, L., et al. (2021). Enhanced photocatalytic degradation and H_2/H_2O_2 production performance of S-pCN/$WO_{2.72}$ S-scheme heterojunction with appropriate surface oxygen vacancies. *Nano Energy, 81*, Article 105671. https://doi.org/10.1016/j.nanoen.2020.105671

Liu, K., Zhang, C., Xu, J., & Liu, Q. (2021). Research advance in gas detection of volatile organic compounds released in rice quality deterioration process. *Comprehensive Reviews in Food Science and Food Safety, 20*, 5802–5828. https://doi.org/10.1111/1541-4337.12846

Liu, K., Zheng, Z., Debliquy, M., & Zhang, C. (2022). Highly-sensitive Volatile Organic Compounds Evaluation by Three-Dimensional $ZnFe_2O_4$/$ZnSnO_3$ Heterostructures and Their Predictive Grain Quality Monitoring. *Chemical Engineering Journal, 453*, Article 139824. https://doi.org/10.1016/j.cej.2022.139824

Meng, S., Li, D., Fu, X., & Fu, X. (2015). Integrating photonic bandgaps with surface plasmon resonance for the enhancement of visible-light photocatalytic performance. *Journal of Materials Chemistry A, 3*, 23501–23511. https://doi.org/10.1039/c5ta06955f

Murthy, A. S. R., Pathak, D., Sharma, G., Gnanasekar, K. I., Jayaraman, V., Umarji, A. M., et al. (2015). Application of principal component analysis to gas sensing characteristics of $Cr_{0.8}Fe_{0.2}NbO_4$ thick film array. *Analytica Chimica Acta, 892*, 175–182. https://doi.org/10.1016/j.aca.2015.08.034

Nandi, A., Nag, P., Saha, H., & Majumdar, S. (2018). Precursor Dependent Morphologies of Microwave Assisted ZnO Nanostructures and their VOC Detection Properties. *Materials Today: Proceedings, 5*, 9831–9838. https://doi.org/10.1016/j.matpr.2017.10.174

Qiao, X., Su, B., Liu, C., Song, Q., Luo, D., Mo, G., et al. (2018). Selective Surface Enhanced Raman Scattering for Quantitative Detection of Lung Cancer Biomarkers in Superparticle@MOF Structure. *Advanced Materials, 30*, 1702275. https://doi.org/10.1002/adma.201702275

Qin, W., Yuan, Z., Shen, Y., Zhang, R., & Meng, F. (2022). Phosphorus-doped porous perovskite $LaFe_{1-x}P_xO_{3-\delta}$ nanosheets with rich surface oxygen vacancies for ppb level acetone sensing at low temperature. *Chemical Engineering Journal, 431*. https://doi.org/10.1016/j.cej.2021.134280

Rafiq, U., Mehraj, O., Lone, S., Wahid, M., & Majid, K. (2020). Solvothermal synthesis of Ag_2WO_4/Sb_2WO_6 heterostructures for enhanced charge transfer properties and efficient visible-light-driven photocatalytic activity and stability. *Journal of Environmental Chemical Engineering, 8*, Article 104301. https://doi.org/10.1016/j.jece.2020.104301

Ren, Y., Li, Y., Wu, X., Wang, J., & Zhang, G. (2021). S-scheme Sb_2WO_6/g-C_3N_4 photocatalysts with enhanced visible-light-induced photocatalytic NO oxidation performance. *Chinese Journal of Catalysis, 42*, 69–77. https://doi.org/10.1016/s1872-2067(20)63631-2

Šetkus, A. (2002). Heterogeneous reaction rate based description of the response kinetics in metal oxide gas sensors. *Sensors and Actuators B: Chemical, 87*, 346–357. https://doi.org/10.1016/S0925-4005(02)00269-1

Shen, Y., Jin, L., Xiao, P., Lu, Y., & Bao, J. (2009). Total phenolics, flavonoids, antioxidant capacity in rice grain and their relations to grain color, size and weight. *Journal of Cereal Science, 49*, 106–111. https://doi.org/10.1016/j.jcs.2008.07.010

Utz, F., Spaccasassi, A., Kreissl, J., Stark, T. D., Tanger, C., Kulozik, U., et al. (2022). Sensomics-Assisted Aroma Decoding of Pea Protein Isolates (Pisum sativum L.). *Foods, 11*. https://doi.org/10.3390/foods11030412

Vermeulen, A. C., Kube, C. M., & Norberg, N. (2019). Implementation of the self-consistent Kröner-Eshelby model for the calculation of X-ray elastic constants for any crystal symmetry. *Powder Diffraction, 34*, 103–109. https://doi.org/10.1017/S088571561900037X

Wang, B., Yu, Q., Zhang, S., Wang, T., Sun, P., Chuai, X., et al. (2018). Gas sensing with yolk-shell $LaFeO_3$ microspheres prepared by facile hydrothermal synthesis. *Sensors and Actuators B: Chemical, 258*, 1215–1222. https://doi.org/10.1016/j.snb.2017.12.018

Wang, F., Liu, Y., Wei, H., Wang, G., Ren, F., Liu, X., et al. (2020). Graphene induced growth of Sb_2WO_6 nanosheets for high-performance pseudocapacitive lithium-ion storage. *Journal of Alloys and Compounds, 839*, Article 155614. https://doi.org/10.1016/j.jallcom.2020.155614

Wang, J., Wang, Z., Huang, B., Ma, Y., Liu, Y., Qin, X., et al. (2012). Oxygen Vacancy Induced Band-Gap Narrowing and Enhanced Visible Light Photocatalytic Activity of ZnO. *ACS Applied Materials & Interfaces, 4*, 4024–4030. https://doi.org/10.1021/am300835p

Wang, X., Lu, J., Han, W., Cheng, P., Wang, Y., Sun, J., et al. (2022). Carbon modification endows WO_3 with anti-humidity property and long-term stability for ultrafast H_2S detection. *Sensors and Actuators B: Chemical, 350*, Article 130884. https://doi.org/10.1016/j.snb.2021.130884

Wang, Z., Cheng, Q., Wang, X., Li, J., Li, W., Li, Y., et al. (2021). Carbon dots modified bismuth antimonate for broad spectrum photocatalytic degradation of organic pollutants: Boosted charge separation, DFT calculations and mechanism unveiling. *Chemical Engineering Journal, 418*, Article 129460. https://doi.org/10.1016/j.cej.2021.129460

Yan, M., Wu, Y., Hua, Z., Lu, N., Sun, W., Zhang, J., et al. (2021). Humidity compensation based on power-law response for MOS sensors to VOCs. *Sensors and Actuators B: Chemical, 334*, Article 129601. https://doi.org/10.1016/j.snb.2021.129601

Yang, C., Yang, X., Li, F., Li, T., & Cao, W. (2016). Controlled synthesis of hierarchical flower-like Sb_2WO_6 microspheres: Photocatalytic and superhydrophobic property. *Journal of Industrial and Engineering Chemistry, 39*, 93–100. https://doi.org/10.1016/j.jiec.2016.05.013

Yao, M. S., Tang, W. X., Wang, G. E., Nath, B., & Xu, G. (2016). MOF Thin Film-Coated Metal Oxide Nanowire Array: Significantly Improved Chemiresistor Sensor Performance. *Advanced Materials, 28*, 5229–5234. https://doi.org/10.1002/adma.201506457

Yau, N. J. N., & Liu, T. T. (1999). Instrumental and sensory analysis of volatile aroma of cooked rice. *Journal of Sensory Studies, 14*, 209–233. https://doi.org/10.1111/j.1745-459X.1999.tb00113.x

Yu, L., Turner, M. S., Fitzgerald, M., Stokes, J. R., & Witt, T. (2017). Review of the effects of different processing technologies on cooked and convenience rice quality. *Trends in Food Science & Technology, 59*, 124–138. https://doi.org/10.1016/j.tifs.2016.11.009

Zhang, P., Li, H., Chen, X., Xiang, R., Hu, H., & Li, C. (2021). Crystal structural and microwave dielectric properties of $Ba_4B'Nb_3O_{12}$ (B′=Yb, Tm, Er, Y, Ho, Dy, Gd) ceramics. *CeramicsInternational, 47*, 12199–12204. https://doi.org/10.1016/j.ceramint.2021.01.067

Zhang, Y., Liu, D., Zhang, Y., Qian, Y., Li, C., Qu, Z., et al. (2022). Highly sensitive photoelectrochemical neuron specific enolase analysis based on cerium and silver Co-Doped Sb_2WO_6. *Biosensors & Bioelectronics, 203*, Article 114047. https://doi.org/10.1016/j.bios.2022.114047

Zhang, Z. J., & Chen, X. Y. (2016). Sb_2MoO_6, Bi_2MoO_6, Sb_2WO_6, and Bi_2WO_6 flake-like crystals: Generalized hydrothermal synthesis and the applications of Bi_2WO_6 and Bi_2MoO_6 as red phosphors doped with Eu^{3+} ions. *Materials Science and Engineering: B, 209*, 10–16. https://doi.org/10.1016/j.mseb.2015.12.003

Zheng, Z., Liu, K., Xu, K., & Zhang, C. (2022). Investigation on microstructure and nonanal sensing properties of hierarchical Sb_2WO_6 microspheres. *Ceramics International, 48*, 30249–30259. https://doi.org/10.1016/j.ceramint.2022.06.298

Zheng, Z., Zhang, C., Liu, K., & Liu, Q. (2022). Volatile Organic Compounds, Evaluation Methods and Processing Properties for Cooked Rice Flavor. *Rice, 15*, 53. https://doi.org/10.1186/s12284-022-00602-3

Zhou, Q., Zeng, W., Chen, W., Xu, L., Kumar, R., & Umar, A. (2019). High sensitive and low-concentration sulfur dioxide (SO_2) gas sensor application of heterostructure NiO-ZnO nanodisks. *Sensors and Actuators B: Chemical, 298*. https://doi.org/10.1016/j.snb.2019.126870